Measurement 281 (2026) 121993

Contents lists available at ScienceDirect

Measurement

journal homepage: www.elsevier.com/locate/measurement

Metrological properties of thin and ultra-thin coating thickness measurement by nanoindentation

Giacomo Maculotti [a,*], Luigi Ribotta [b], Gianfranco Genta [a], Maurizio Galetto [a]

[a] Department of Management and Production Engineering, Politecnico di Torino, Corso Duca degli Abruzzi 24, 10129 Turin, Italy
[b] Applied Metrology and Engineering Division, Istituto Nazionale di Ricerca Metrologica (INRiM), Strada delle Cacce 91, 10135 Turin, Italy

ARTICLE INFO

Keywords:
Thickness measurement
Coating
Nanoindentation
Calibration
Uncertainty
Traceability

ABSTRACT

Coatings enable the engineering of surface properties, and thickness is one of the most important design parameters to control function and integration within the application environment. Ultra-thin coatings, i.e., those with thicknesses smaller than 100 nm, find applications in the electronics and biomedical fields. However, measurement of the thickness is often challenging. Innovatively, this work demonstrates the applicability of a recent nanoindentation-based approach in measuring the thickness of hard, ultra-thin coatings. Additionally, the work innovatively discusses the traceability of the thickness measurement, highlighting its metrological properties in terms of accuracy and measurement uncertainty. Additionally, a comparison with other primary traceable techniques is provided, complemented by a sensitivity analysis of measurement accuracy to coating thickness. Results show a relative expanded uncertainty of about 15% of the measurement, and an excellent accuracy with a bias with respect to directly traceable measurements that is not statistically significant. This work contributes to demonstrate the applicability of nanoindentation for coating thickness measurement on a wide range of thickness and composition.

1. Introduction

Coatings represent an essential surface technology capable of functionalizing and engineering surface properties [1]. Applications span a wide range of fields, from traditional manufacturing [2,3] to cutting-edge technologies [4,5]. Advanced coatings are used in the automotive sector for anti-glare, environmentally sustainable and protective painting, infotainment devices, electronics [6], and power electronics related to electrification [7]. In aerospace, extensive research has been performed on coatings for thermal control, i.e., showing stability of composition, mechanical and functional properties through a wide range of temperature, typically coupled with high resistance to radiation and solar absorptivity, and for optical applications, e.g., capable of increasing reflectance or controlling transmittance to filter received wavelengths [8]. Wear-resistant coatings have been widely researched to extend the durability of cutting tools [9] and mechanical couplings, such as bushings with solid lubricants [10–12]. Widespread applications can also be found in bioengineering, where biocompatibility, e.g., through the use of hydroxyapatite or polymers [10], antibacterial [11], and antimicrobial [12] properties, as well as improved osteointegration [13], can be provided by high-performance coatings in biomedical applications. Advanced high-performance coatings are widely applied in energy applications to enhance energy harvesting through texturing [14], passivation [15], and efficiency [13]. Finally, quantum sensors based on ultra-thin films, i.e., coatings with thickness smaller than 100 nm, are being increasingly studied as gas concentration sensors [14] and temperature detectors [15].

Coating thickness is a functional property that controls both durability and functionality of the coated system. Coatings for contact and wear applications benefit from layers thicker than 1 μm to extend the useful life of the application, e.g., cutting tools [9], bushings [11], with a specific dependence of the stress tensor in the substrate on the coating thickness [16]. Similarly, corrosion resistance is dependent on coating thickness [17]. Furthermore, the push towards miniaturisation, biological and bioengineering, and quantum technology applications is requiring increasingly thinner coatings. In electronics and energy applications, wafer passivation coatings have a typical thickness not exceeding 100 nm. Advances in quantum technology have shown that for thinner coatings, i.e., a few tens of nanometers thick, vacancies and interstitial defects enable the generation of unique electronic and optical responses, which are applicable as sensors and detectors [18]. Within these fields, thickness has been proven to be highly correlated with

* Corresponding author.
E-mail address: giacomo.maculotti@polito.it (G. Maculotti).

https://doi.org/10.1016/j.measurement.2026.121993
Received 9 March 2026; Received in revised form 9 May 2026; Accepted 20 May 2026
Available online 22 May 2026
0263-2241/© 2026 The Author(s). Published by Elsevier Ltd. This is an open access article under the CC BY-NC-ND license (http://creativecommons.org/licenses/by-nc-nd/4.0/).

crystallinity and purity [5,19], which in turn affect permittance and impedance [20], conductivity [21], structural and optical properties [22], and on magnetic properties [23,24] of the coating, thus ultimately controlling the sensitivity of the sensor based on such a technology. In bioengineering, coating thickness has been shown to affect the adsorption and release of molecules, as well as control flow in microfluidic devices for controlled drug release [25,26]. Similarly, a significant dependence on the thickness of antimicrobial and biocompatibility properties was shown in several cases [27,28].

Accordingly, measuring coating thickness is of primary importance, and advanced applications pushing towards ultra-thin coatings, i.e., thinner than 100 nm, are challenging conventional methods. Several approaches are available, are discussed in the following and summarized in Table 1.

Destructive methods, which rely on cross-sectioning and inspection by optical microscopy or scanning electron microscopy (SEM), are largely used measurement approaches. However, cross-sectioning can be highly challenging in obtaining perpendicular fracture surfaces and typically introduces damage that might alter the structure and thickness of the coating itself [29]. Thus, they are conventionally applied for coatings with a thickness of at least 500 nm, and suitable mechanical properties. Moreover, the inspection of optical microscopy or SEM can introduce sine errors and depth of field-related errors, which are very hard to compensate [29,30].

Thus, methods that do not require cross-sectioning are largely preferred; however, they are more expensive. High-energy wavelength non-destructive methods are typically extremely expensive and complex. Alternatives are X-ray diffraction for thicker coatings, i.e., thicker than 1 μm, and X-ray fluorescence for thin and ultra-thin coatings [29].

Conversely, optical methods are less expensive. Foremost, optical ellipsometry is a widely employed technique in industry due to its simplicity; however, it is limited to thicknesses greater than 100 nm and requires a transparent layer, thus showing strong limitations for metallic coatings [31]. Moreover, optical ellipsometry is highly sensitive to fitting methods and fitting parameters, thus further limiting its robustness [31]. Further optical methods are available, proving excellent results. Methods requiring an extremely complex measurement setup, for example, are based on photothermal [32] or ultrasound [33] generated by lasers. Conversely, hyperspectral imaging [34] and surface topography microscopes, e.g., confocal microscopes and coherence scanning interferometers, are limited to transparent coatings [35,36].

Table 1
Summary of main coating thickness measurement methods.

Method	Destructive	Ease of use	Cost	Limitations
Cross-section + Optical microscope	Yes	High	Low	Relevant sine errors, cross-sectioning can critically damage the interface [29,30].
Cross-section + SEM	Yes	Low	High	
X-ray Diffraction	No	Low	High	Applicable to thickness greater than 1 μm [29].
X-ray fluorescence	No	Low	High	Applicable to thickness smaller than 1 μm [29].
Ellipsometry	No	Medium	Medium	Applicable to thickness greater than 100 nm, to transparent coating [31].
Laser based effect	No	Low	High	Extremely complex setup [32,33].
Scanning Probe Microscopy	No	Medium	High	Requires a step, compensation of deformation due to the mechanical contact [37].
Nanoindentation	Yes (locally)	Medium	Medium	Only demonstrated to hard coatings and thickness greater than 500 nm.

Convenient and directly traceable approaches are represented by contact stylus (CS) and scanning probe microscopy (SPM). These allow for measuring coating thickness as step heights, provided an uncoated substrate area is available in continuity with the coating. National metrological institutes (NMIs) perform directly traceable measurements by interferometric measurements of the axes motion. This is typically obtained by phase grating interferometric contact stylus (PGI-CS) and by closed-loop atomic force microscopes (AFM) with interferometric axes [29]. On the one hand, approaches can cover a wide range of thickness. On the other hand, they are liable to introduce measurement errors in the step, thus requiring extensive lateral scanning, which increases the measurement time [29]. Furthermore, being contact methods, they require complex modelling to account and compensate for the coating's mechanical response, particularly critical for polymer and bio-materials [37].

Among the other measurement techniques, an approach based on nanoindentation has been recently proposed [38]. The approach couples the simplicity of the experimental setup with the capability to manage a wide range of materials, thereby overcoming limitations set by transparency, composition, and mechanical response. It does not require any sample preparation, such as cross-sectioning, while being capable of managing multi-layer coatings [38]. However, the method was only tested on relatively thick coatings, i.e., having a thickness of at least 500 nm, and a thorough discussion of the metrological characteristics was missing.

Innovatively, this work aims to demonstrate the applicability of the nanoindentation-based coating thickness measurement method to ultra-thin coatings, to discuss traceability, and to evaluate the accuracy and measurement uncertainty of the method across a wide range of coating thickness. Additionally, an analysis of the metrological characteristics' sensitivity to the measured thickness will be performed, and a comparison with directly traceable methods for thickness measurement will be conducted.

The rest of this paper is structured as follows. Section 2 expands the description of the method introduced in [38], and describes the experimental setup. Section 3 discusses traceability, highlights the approach for uncertainty evaluation, and presents the experimental methodology for evaluating the main metrological characteristics. Section 4 presents and discusses the results, and Section 5 finally draws the conclusions.

2. Methodology

Nanoindentation is a depth-sensing hardness measurement technique. During an indentation cycle, a force is applied to a sample by means of an indenter, and both the applied force F and the indenter penetration depth h are continuously measured [39,40]. The analysis of the indentation curve (IC), i.e., $F(h)$, allows evaluating the mechanical characteristics of the surface layer. In particular, most typically evaluated properties are the indentation hardness H_{IT} and the indentation modulus E_{IT}, which estimates the Young modulus of the sample. These are evaluated thanks to the correlation between the projected area $A_p(h_{c,max})$ of the indenter surface in contact with the sample at the maximum corrected penetration depth, as described in Eq. (1) and Eq. (2):

$$H_{IT} = \frac{F_{max}}{A_p(h_{c,max})} \tag{1}$$

$$E_{IT} = \frac{1-\nu_s^2}{\frac{2\sqrt{A_p(h_{c,max})}}{S\sqrt{\pi}} - \frac{1-\nu_i^2}{E_i}}, \tag{2}$$

where, F_{max} is the maximum applied force, ν_s and ν_i are the Poisson's ratio of the sample and of the indenter, respectively, and E_i is the Young's modulus of the indenter. S is the sample contact stiffness, which is evaluated from the stiffness model of the indenter-sample system as a series of springs, having a total compliance C_{Tot} resulting from Eq. (3.1),

$$C_{Tot} = \frac{1}{S_m} = \frac{1}{S} + C_f \tag{3.1}$$

$$S_m = \left.\frac{dF}{dh}\right|_{h=h_{max}}, \tag{3.2}$$

where C_f is the frame compliance and S_m is the measured contact stiffness, as in Eq. (3.2). The measured penetration depth $h_{c,max}$ is corrected for zero error h_0, for the elastic deformation of the indentation machine $C_f F_{max}$, and for the elastic deformation of the sample $\varepsilon \frac{F_{max}}{S}$, so that it results in:

$$h_{c,max} = h_{max} - h_0 - C_f F_{max} - \varepsilon \frac{F_{max}}{S}, \tag{4}$$

where ε is a geometric factor depending on the indenter geometry, e.g., for a Berkovich indenter, it is $\varepsilon = 0.75$.

2.1. Measurement of coating layer thickness by nanoindentation

Considering a multilayered coating with n layers and a substrate, the indentation of such a material induces a stress tensor that involves a volume of material depending on the penetration depth. Accordingly, for each i-th layer, with $i \in [1, \cdots, n]$, a functional thickness t_{fi} and a layer thickness t_i can be distinguished. The former, i.e., t_{fi}, represents a penetration depth such that the stress tensor is still limited to the i-th indented layer and is not influenced by the next, i.e., the $i+1$-th, layer. The latter, i.e., t_i, is the depth of the physical interface between the i-th and the $i+1$-th layer. Fig. 1(a-b) shows a conceptual schematic representation, following the discussed modelling according to [38]. For penetration depths larger than 10% of the layer thickness, the mechanical response of the material depends both on the indented layer and the material layer below [41,42], i.e. a first approximation for the functional thickness is obtained as $t_{fi} \sim 0.1 t_i$.

By means of continuous multi-cycle (CMC) indentation, i.e. the application of indentation cycles with increasing F_{max} in the same location, it is possible to map any surface property, e.g., $M = \{H_{IT}, E_{IT}\}$, as a function of the maximum corrected penetration depth. In the simplest case of a monolayered coating, i.e., $n = 1$, the relationship $M(h)$ shows two plateaux and a transient, see Fig. 1(c). The constant regions describe ranges of penetration depths where the material response is affected only by the indented layer, i.e. for $h < t_{fi}$ and for $h > t_i$. For $h \in [t_{fi}; t_i]$, the transient reflects the superposition of the mechanical response of the layer and substrate due to the deformed volume of material by the stress tensor, and by specific material structure and composition, also dependent on the particular deposition process phenomena, e.g., the presence of a continuous gradient due to solid state diffusion between the layer and the substrate [43]. Most typically, sigmoid functions can model the mathematical relationship $M(h_{c,max})$. Sigmoid functions describe a family of models whose flexibility depends on the number of model parameters. A three-parameter logistic function or a four-parameter sigmoid can model the mathematical relationship $M(h_{c,max})$:

$$M = g(h_{c,max}; \boldsymbol{\vartheta}) = \frac{\vartheta_1}{1 + e^{-\vartheta_2 (h_{c,max} - \vartheta_3)}} \tag{5.1}$$

$$M = g(h_{c,max}; \boldsymbol{\vartheta}) = \vartheta_1 + \frac{\vartheta_2 - \vartheta_1}{e^{\frac{h_{c,max} - \vartheta_3}{\vartheta_4}}}, \tag{5.2}$$

where sigmoid parameters $\boldsymbol{\vartheta}$ can be estimated by nonlinear least-square fitting [38,44]. The specific choice of the model depends on data, and conventional goodness-of-fit tests on regression residuals are required to verify the statistical robustness and adequateness of the selected model. A practical suggestion for model selection depends on whether data related to the functional layer thickness are available. In that case, a four-parameter model of Eq. (5.2) can be applied. Conversely, if the particular combination of the minimum applicable F_{max} and material properties results in $h_{c,max}$ significantly larger than the 10% of the nominal layer thickness, a simplified and truncated form of the model, i.e., the logistic regression of Eq. (5.1), can be preferred. Alternatively, shallower indentations could be obtained for the same F_{max} using a spherical indenter.

From a statistical perspective, the distribution of a given material property response M can be considered as the convolution of the property response distributions of each layer that superposes. Accordingly, it can be modelled as a Gaussian Mixture Model (GMM):

$$M \sim GMM(\boldsymbol{\theta}) = GMM(\boldsymbol{\mu}, \boldsymbol{\Sigma}; \boldsymbol{\pi}) = \sum_{k=1}^{2n+1} \pi_k N(\mu_k, \sigma_k^2) = \sum_{i=1}^{n+1} \pi_i N(\mu_i, \sigma_i^2) + \sum_{j=1}^{n} \pi_{j/j+1} N\left(\mu_{j/j+1}, \sigma_{j/j+1}^2\right), \tag{6}$$

having a probability density function f_M, detailed in Eq. (7);

$$f_M = f_M(m|\boldsymbol{\theta}) = \sum_{k=1}^{2n+1} \pi_k f_{M,k}(m|\{\mu_k, \sigma_k^2\}) \tag{7}$$

The model mixture in Eq. (6), written for n coating layers and the substrate, i.e., the $n+1$ material layers, caters for functional layers having mean and variance μ_i and σ_i^2, and for transition layers from the j-th to the $j+1$-th functional layer, with mean and variance $\mu_{j/j+1}$ and $\sigma_{j/j+1}^2$. The parameters of the GMM, i.e. the latent mixture components parameters $\boldsymbol{\mu}, \Sigma$ and the mixture weights π can be estimated by deconvolving the empirical GMM. In particular, given the k-th mixture component, the relevant latent parameters μ_k, σ_k^2 and π_k can be estimated by the expectation maximisation (EM) algorithm [45], subjected to the constraints $0 < \pi_k < 1$, $\sum_{k=1}^{2n+1} \pi_k = 1$ [46].

GMM are conventionally used as unsupervised learning classifiers [46]. Classification can be exploited to assign any observations m, i.e., a realisation of the material property response M, to a component of the mixture. The classification can be performed by hard clustering, i.e., by identifying the component z_m of the mixture that maximises the maximum a-posteriori probability (MAP) that the observation m is a realisation of the k-th latent mixture component:

$$p(z_m = k|m, \boldsymbol{\theta}) = \frac{\pi_k f_{M,k}(m)}{f_M(m|\boldsymbol{\theta})} \tag{8}$$

$$z_m = \underset{k}{\operatorname{argmax}} \{p(z_m = k|m, \boldsymbol{\theta})\} = \underset{k}{\operatorname{argmax}} \left\{\log\left(f_{M,k}(m)\right) + \log(\pi_k)\right\}. \tag{9}$$

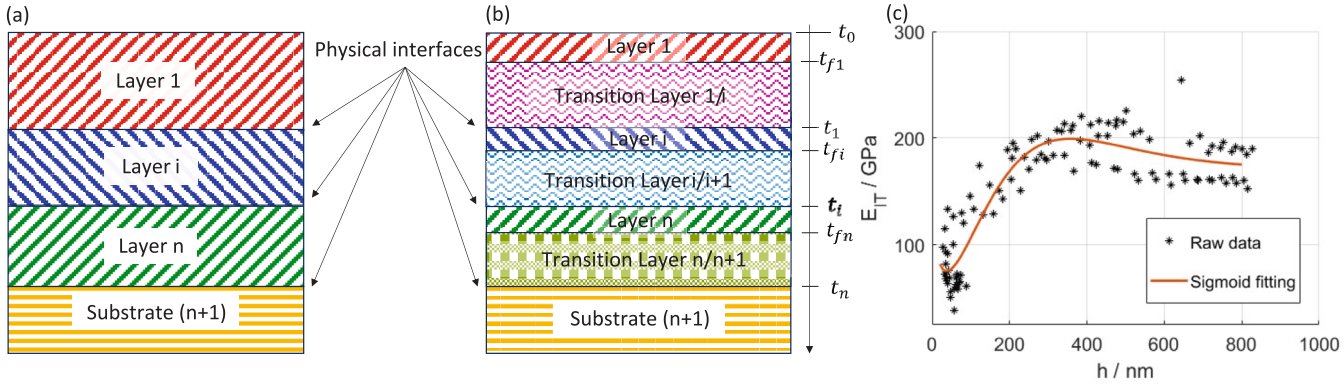


Fig. 1. (a) Conceptual representation of a multi-layer coating system. (b) Conceptual representation highlighting functional thickness t_{fi}, physical interfaces, and transition layers. (c) Typical depth-profiling of E_{IT} for a monolayer coating obtained by CMC nanoindentation of a 550 nm SiO_2/Si<1 0 0>: notice the two plateau for h < 50 nm related to the coating, and for h > 550 nm related to the substrate [38].

Indeed, misclassification errors may occur. It is in particular useful to set a maximum risk of error of type I for the selected class, i.e., for the predicted mixture component, α_k. In particular, it can be defined as the probability of performing a classification error for the observation m, assumed to be a realisation of the k-th mixture component, i.e.,

$$\alpha_k = p(z_m \neq k | m \in k, \boldsymbol{\theta}) = 1 - p(z_m = k | m, \boldsymbol{\theta}) \tag{10}$$

It can be associated with a quantile M_k^* of the k-th mixture component that satisfies a classification confidence level $P_k = 1 - \alpha_k$. Accordingly, two situations can be distinguished. If the i-th layer is harder than the $i + 1$-th layer, an increasing trend of $M = g(h_{c,max}; \boldsymbol{\vartheta})$ results, and the two quantiles for the functional layer M_{fi}^* and the physical interface M_i^* can be written as:

$$M_{fi}^* = \min\{m : p(k = 2i - 1 | m, \boldsymbol{\theta}) = 1 - \alpha_{2i-1}\} \tag{11}$$

$$M_i^* = \max\{m : p(k = i + 2 | m, \boldsymbol{\theta}) = \alpha_{i+2}\}. \tag{12}$$

In a dual way, if the i-th layer is softer than the $i + 1$-th layer, a decreasing trend of $M = g(h_{c,max}; \boldsymbol{\vartheta})$ results, and the threshold material properties can be written as:

$$M_{fi}^* = \max\{m : p(k = 2i - 1 | m, \boldsymbol{\theta}) = 1 - \alpha_{2i-1}\} \tag{13}$$

$$M_i^* = \min\{m : p(k = i + 2 | m, \boldsymbol{\theta}) = \alpha_{i+2}\} \tag{14}$$

Once the thresholds M^* have been evaluated, it is possible to estimate the associated penetration depth by inverting the model $g(h_{cmax}, \boldsymbol{\theta})$ defined in Eq. (5), i.e.:

$$t_{M,fi}^* = g^{-1}\left(M_{fi}^*\right) \tag{15}$$

$$t_{M,i}^* = g^{-1}\left(M_i^*\right) \tag{16}$$

2.1.1. Data fusion

According to Eq. (15) and Eq. (16), for each of the material properties M evaluated by nanoindentation, it is possible to estimate a layer thickness. This allows for leveraging the redundancy of information to improve measurement accuracy and reduce the dispersion by data fusion (DF). In particular, it is possible to combine any thickness estimation $t_{M,i}^*$ from different material properties by means of the inverse variance weighting, i.e.,

$$\widehat{t_{DF,i}^*} = \frac{\sum_{w=1}^{\#M} t_{w,i}^* \Big/ u^2\left(t_{w,i}^*\right)}{\sum_{w=1}^{\#M} 1 \Big/ u^2\left(t_{w,i}^*\right)} \tag{17}$$

$$u^2\left(\widehat{t_{DF,i}^*}\right) = \frac{1}{\sum_{w=1}^{\#M} 1 \Big/ u^2\left(t_{w,i}^*\right)}, \tag{18}$$

where $\#M$ is the number of evaluated material properties, and Eq. (17) describes the average thickness $\widehat{t_{DF,i}^*}$ estimated by DF, and Eq. (18) its variance $u^2\left(\widehat{t_{DF,i}^*}\right)$. The DF weights estimations obtained by different material properties $t_{M,i}^*$ by their combined uncertainties $u^2\left(t_{M,i}^*\right)$. The method to estimate the $u^2\left(t_{M,i}^*\right)$ will be described in Section 3.3.

2.2. Experimental setup

This work aims to demonstrate the applicability of the nanoindentation-based method for measuring the thickness of coating layers for ultra-thin coatings. Accordingly, four sets of coatings were deposited by physical vapour deposition. The coatings were deposited on a Si<1 0 0>wafer substrate [47] and characterised in [48]. Two coatings were deposited, i.e., a SiO_2 matrix functionalized by silver nanoparticles (SiO_2AgNP/Si<1 0 0>), and a ZrO_2 matrix functionalized by silver nanoparticles (ZrO_2AgNP/Si<1 0 0>). The coatings are typically applied to air filters to leverage the antibacterial and antiviral properties provided by the AgNP functionalization [27]. The deposition was performed considering durations of 30′ and 60′ to obtain coatings with different thicknesses. The deposition was performed for the SiO_2AgNP/Si<1 0 0>targeting the Si target with a 200 W radio frequency and the silver target with a 5 W direct current, and for ZrO_2AgNP/Si<1 0 0>targeting the Zr target with a 250 W radio frequency and the silver target with a 4 W direct current. The manufacturing process was performed in Argon atmosphere at a pressure of 5.5 dPa [49,50]. The deposition was performed while half of the substrate was covered by an inert polymeric film, allowing for a step height to be obtained after the deposition by simply removing the film.

Nanoindentation experiments were performed by a state-of-the-art STeP6 Anton Paar indentation platform, by means of an NHT^3 nanoindenter, shown in Fig. 2(a), in the metrological room of the Mind4Lab of Department of Management and Production Engineering of Politecnico di Torino. The equipment features a calibrated force–displacement three-plate capacitive transducer allowing a force application in the range (0.1–500) mN, with a resolution of 20 nN, a noise floor of 1 μN, and a reproducibility of 3 μN. The displacement is measured by the same sensor in a range of 40 μm with a resolution of 0.01 nm, a noise floor of 0.3 nm, and a reproducibility of 1 nm, which limits the ideal minimum measurable penetration depth.

The instrument was equipped with a Berkovich indenter, and nanoindentations were performed, implementing a 4 × 4 matrix of

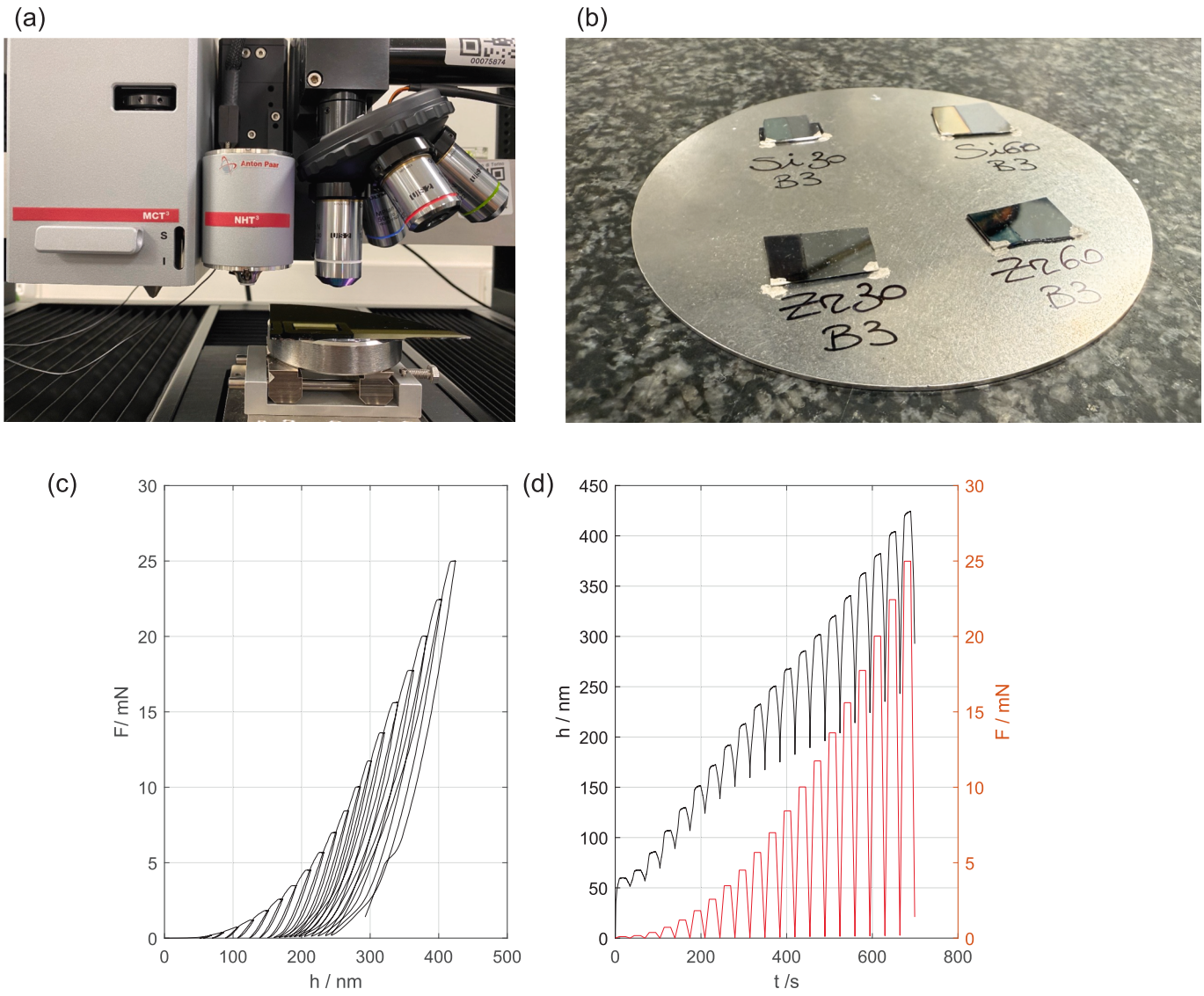


Fig. 2. (a) Anton Paar NHT^3 nanoindenter. (b) the four coated samples, where it is possible to distinguish the coated step from the substrate (darker region). (c) typical indentation curve, *F(h)*, for a continuous multi-cycle indentation. (d) raw measured penetration depth (*h*) in black (left axis) that results from the applied force (*F*) in red (right axis) for a continuous multi-cycle indentation. (c-d) refer to an indentation on SiO_2AgNP/Si<1 0 0>deposited for 60′.

continuous multi-cycle indentations for each of the four coated samples, shown in Fig. 2(b). Each indentation consisted of a set of 20 cycles quadratically spaced, to improve resolution at shallow depths, between 0.1 mN and 25 mN. Each cycle consisted of loading, holding, and unloading with durations of 10 s, 15 s, and 10 s, respectively, as shown in Fig. 2(c) and Fig. 2(d).

Accordingly, the model proposed in Section 2.1 considers one layer, i.e., $n = 1$, and the coating thickness t_c, i.e. the physical interface, results as $t_c = t^*_{M,2}$. The EM algorithm was initialized by a k-means++ algorithm [51], rather than performing an initialization with random seed, performing 50 independent replications and selecting the result maximizing the negative Log-Likelihood.

3. Metrological properties

The second focus of this paper is to provide a discussion and evaluation of the metrological properties of the nanoindentation-based method for coating thickness measurements. In this section, traceability and methodology for evaluating bias and uncertainty are discussed.

3.1. Traceability

The traceability of the thickness measurement is established through the calibration of the nanoindentation instrument. In particular, the force–displacement sensor was calibrated according to the requirements of ISO 14577–2 [52]. The calibration of the force–displacement sensor yielded a bias of less than 1% for both the force and the penetration depth measurements [52].

Furthermore, the correction of systematic errors associated with the finite stiffness of the indentation instrument and of the non-ideal geometry of the indenter requires calibration of the frame compliance C_f and of the area shape function, $A_p(h_{c,max})$, parameters, respectively. The calibration of frame compliance and area shape function parameters was performed using the two-material method and the single-step procedure described in [51], which improves upon the standard approach outlined in ISO 14577-2. This method was accompanied by a bootstrap uncertainty evaluation to account for the reproducibility of the calibration indentation dataset [53–55]. The procedure exploited calibrated reference materials of SiO_2 and tungsten. The calibration was performed in the range from 25 nm to 215 nm. The traceability of the frame

compliance and area shape function calibration leverages the calibration of the Young modulus and Poisson's ratio of the calibrated reference materials by frequency resonance performed at NPL. The calibration of the frame compliance allows for correcting the measured penetration depth according to Eq. (4), resulting in relative expanded uncertainties of 2% and 6% for the indentation modulus and indentation hardness, respectively [53]. Last, systematic errors in the penetration depth measurement due to thermal drift at the indenter and sample contact are compensated, as per ISO 14577-1 [40], by evaluating the thermal penetration drift rate by a stabilization performed before the start of each indentation cycle.

3.2. Measurement uncertainty

Measurement uncertainty is evaluated according to the Guide for the expression of Uncertainty in Measurement (GUM) by applying the Law of Propagation of Uncertainty (LPU) [56]. Specifically, the combined variance of the measured thickness by the nanoindentation-based method, $u^2\left(t^*_{M,i}\right)$, can be written as:

$$u^2\left(t^*_{M,i}\right) = c^T[VCV]c = \begin{bmatrix} \left.\frac{\partial g^{-1}(M;\vartheta)}{\partial \vartheta}\right|_{\hat{\vartheta}} \\ \left.\frac{\partial g^{-1}(M;\vartheta)}{\partial M}\right|_{M^*_k} \\ 1 \\ 1 \end{bmatrix}^T \begin{bmatrix} \Sigma_\vartheta & 0 & 0 & 0 \\ 0 & u^2(M)+MSE & 0 & 0 \\ 0 & 0 & u^2(h) & 0 \\ 0 & 0 & 0 & u^2_{EM,init}+u^2_{GMM,reprod} \end{bmatrix} \begin{bmatrix} \left.\frac{\partial g^{-1}(M;\vartheta)}{\partial \vartheta}\right|_{\hat{\vartheta}} \\ \left.\frac{\partial g^{-1}(M;\vartheta)}{\partial M}\right|_{M^*_k} \\ 1 \\ 1 \end{bmatrix}, \tag{19}$$

where c is the array of sensitivity coefficients, i.e., of partial derivatives of the metrological model, and $[VCV]$ is the variance–covariance matrix of the uncertainty contributions. These account for: the variance–covariance matrix Σ_ϑ of the estimates of model parameters $\hat{\vartheta}$ obtained by the nonlinear regression, the regression residuals mean squared error *MSE*, the metrological characteristics of the nanoindentation system, and for the variability due to the classification algorithm. The metrological characteristics of the nanoindentation system describe the traceability and the reproducibility. The traceability is propagated as the standard uncertainty of the evaluated mechanical property, i.e. $u^2(M)$, from the relative contributions estimated in calibration (see Section 3.1). In particular, $u^2(M)$ is evaluated by applying the LPU to the Eqs. (1) and (2) and propagating the relevant contributions of the maximum applied force, the projected contact area, which includes contributions of the frame compliance and the area shape function calibration, the contact stiffness, the Poisson's ratio of both the sample and the indenter, and the Young modulus of the indenter (the last three propagated as type B contributions) [53,57,58]. The reproducibility of the testing equipment is associated with the penetration depth measurement, i.e., $u^2(h)$, and estimated empirically as the variance of the measured maximum penetration depths. Additional contribution to the reproducibility is modelled by the *MSE*, which includes contributions to measurement uncertainty due to the sample uniformity, surface roughness, and any effect of small wear of the indenter tip during the replicated tests. Uncertainty contribution due to the thermal drift compensation are neglected due to the small uncertainty of the thermal penetration drift rate. Further, contributions from the GMM classification can be considered. First, systematic errors due to the initialization method for the EM algorithm, i.e., $u^2_{EM,init}$, can be considered. Second, random classification error, i.e., $u^2_{GMM,reprod}$, can be modelled. The former is evaluated by performing 100 independent evaluations initializing the EM algorithm with both the k-means++ algorithm and a random seed, computing the respective average and evaluating the variance contribution as:

$$u^2_{EM,init} = \frac{\left(\overline{t^*_{M,i,k-means++}} - \overline{t^*_{M,i,random}}\right)^2}{3}. \tag{20}$$

The latter is evaluated as the variance of the 100 replications obtained initializing the EM algorithm with the k-means++ algorithm. According to the previous discussion, all contributions are propagated as type A contributions.

Finally, measurement uncertainty is evaluated considering a confidence level of 95%, and a coverage factor k_{t^*} evaluated as the relevant quantile of a t-Student distribution with ν_t degrees of freedom evaluated by means of the Welch-Satterthwaite formula [56]. It follows that $U\left(t^*_{M,i}\right) = k_{t^*} \bullet u\left(t^*_{M,i}\right)$. Last, it is worth emphasising that the formulation of Eq. (19) applies to both the functional and physical interface layer thicknesses. A breakdown of uncertainty evaluation is available in the annex highlighting contributions and degrees of freedom.

3.3. Measurement accuracy

The accuracy of the thickness measurement was assessed by evaluating systematic differences with respect to primary and directly traceable thickness measurements of the coating step height performed by phase grating interferometric contact stylus (PGI-CS) and atomic force microscopy (AFM).

PGI-CS measurements were performed by the Nanometrology and Surface Metrology laboratory at the Italian National Metrological Institute (INRiM) with a Taylor Hobson Form Talysurf PGI Novus S10, shown in Fig. 3(a), having a calibration measurement capability of $U_{CMC,95\%} = \sqrt{1\text{nm}^2 + \left(4.6 \times 10^{-3}\right)^2 \bullet Z^2}$, where Z is the measured step height in nanometres [59]. For each sample, 20 profiles across the step length were measured, and the related step height t_{PGI-CS} was evaluated as per ISO 5436–1 [60]. The sample average $\overline{t_{PGI-CS}}$ and the sample standard deviation $s(t_{PGI-CS})$ of the twenty replications were estimated as the reference calibrated value by the PGI-CS and as the reproducibility contribution of the calibration. Accordingly, the standard uncertainty of the PGI-CS step height measurement was estimated by combining the traceability and the reproducibility [56], i.e.

$$u_{PGI-CS} = \sqrt{\left(\frac{U_{CMC,95\%}}{2}\right)^2 + s^2(t_{PGI-CS})} \tag{21}$$

Accuracy is evaluated as bias with respect to the primary traceable measurements, i.e.

$$e_{PGI-CS} = t_c - t_{PGI-CS} \tag{22}$$

Relative accuracy, i.e. $e_{PGI-CS\%} = e_{PGI-CS}/t_c$, is also reported, and the

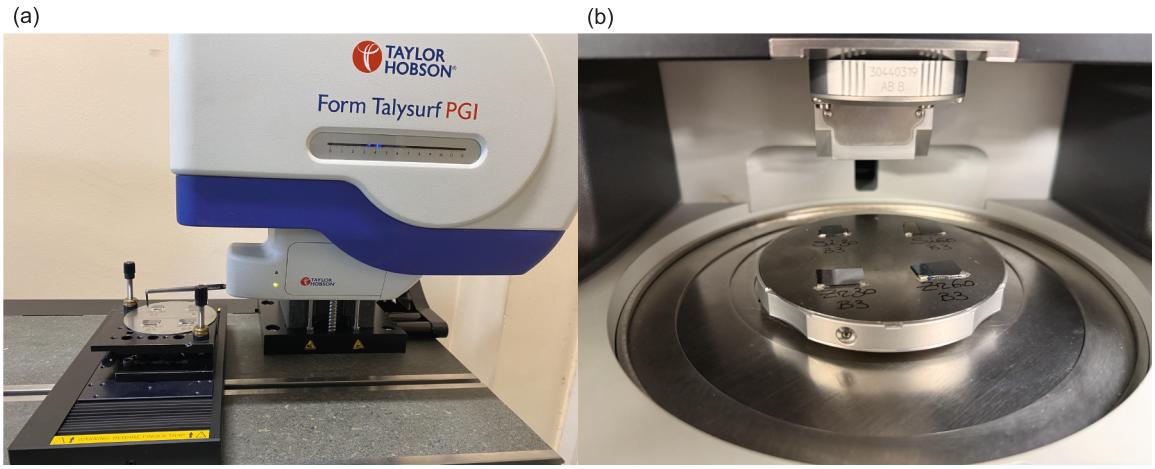


Fig. 3. Directly traceable measuring instruments used to provide reference coating thickness measurements: (a) Phase Grating Interferometric Contact Stylus and (b) Atomic Force Microscope.

statistical significance of the bias is investigated by a hypothesis test on the mean based on the t-Student distribution, with a null hypothesis H_0 : $t_c = t_{PGI-CS}$, and estimating the score of the test as

$$t_{exp} = \frac{t_c - t_{PGI-CS}}{\sqrt{u^2(t_c) + u^2_{PGI-CS}}}\, t_\nu, \tag{23}$$

where t_ν is a t-Student distribution with ν degrees of freedom evaluated by means of the Welch-Satterthwaite formula [56], considering 19 degrees of freedom for the PGI-CS and ν_{t^*} degrees of freedom for the nanoindentation-based thickness evaluation. The degrees of freedom for the PGI-CS results from applying the Welch-Satterthwaite formula to the Eq. (21), considering the step height CMC is low and evaluated with 130 degrees of freedom [59].

Additionally, compatibility investigation of the thickness measurement method based on nanoindentation with AFM step height measurements was addressed. Coating step height measurements were performed using a closed-loop AFM, see Fig. 3(b), installed in the metrological room of the Mind4Lab at Department of Management and Production Engineering of Politecnico di Torino. The measurement noise of the AFM was calibrated and was smaller than 0.08 nm. Because the maximum measured area is (100 × 100) µm, and the manufacturing resulted in a slurred step wide about 400 µm due to the presence and subsequent removal of the inert polymeric film, the step height could not be measured directly. Conversely, six pairs of topographies were measured for each sample on both the coating and the substrate at a distance of at least 1 mm from the step. The AFM enables relative positioning along the cantilever's z-axis, which was exploited to estimate the step height. Specifically, measured pairs of topographies were levelled line by line [61], then the average absolute surface height was measured, and the step height resulted as:

$$t_{AFM} = \overline{z_{coating}} - \overline{z_{substrate}}. \tag{24}$$

The sample average of the six measurements is considered a traceable measurement of the coating thickness $\overline{t_{AFM}}$, and the sample standard deviation $s(t_{AFM})$ estimates the standard uncertainty, assuming that reproducibility is the most significant contributing factor. The compatibility of the method based on nanoindentation, described in Section 2, with AFM measurements was investigated using a hypothesis test on the mean based on the t-Student distribution, similar to Eq. (23), with degrees of freedom for the difference combining the 5 degrees of freedom for the AFM and the ν_t degrees of freedom for the nanoindentation based measurement through the Welch-Satterthwaite formula.

Details for the evaluation of the measurement uncertainty for both the PGI-CS and the AFM thickness measurement are available in the annex.

3.3.1. *Sensitivity of accuracy to measured coating thickness*

The sensitivity accuracy e_{PGI-CS} and of the relative accuracy $e_{PGI-CS\%}$ will be studied as a function of reference coating thickness. In order to provide a thorough perspective on the metrological performances of the nanoindentation-based thickness measurement, data obtained in the present work relevant to ultra-thin coatings will be complemented with data from [38] pertaining to thicker coatings, namely a SiO_2/Si<1 0 0>thick (566 ± 17) nm and a PTFE + Pb/Bronze thick (50120 ± 19750) nm. The reference thickness is measured, respectively, by X-ray diffraction and a metallographic optical microscope [38].

4. Results and discussion

The deposited coatings were first characterised by directly traceable methods to evaluate the reference thickness. Table 2 shows the results obtained following the methodology outlined in Section 3.3, details of the uncertainty propagation are available in the annex from Table A2 to Table A9. As can be appreciated, a wide range of ultra-thin and thin coatings were manufactured by sputtering. A lack of statistical compatibility between the AFM and the PGI-CS measurements could not be highlighted by a hypothesis test on the mean based on the t-Student distribution, and the p-values are reported in Table 2. The uncertainty of the AFM is slightly worse than those of the PGI-CS due to the high sensitivity to the effect of local topography. This result confirms the methodology introduced in Section 3.3, to rely on PGI-CS measurements for accuracy evaluation of the nanoindentation-based method. Additionally, AFM measurements were exploited to provide an indication of the surface roughness, resulting for the four coatings, respectively, for

Table 2
Coating thickness measurement by directly traceable methods. Mean and expanded uncertainty (confidence level of 95%). Details for uncertainty propagation in the annex. Degrees of freedom ν and p-value of a t-Student hypothesis test to test compatibility of AFM and PGI-CS measurements.

Material	AFM	PGI-CS	υ	p-value
SiO_2AgNP/Si<1 0 0>30′	(88.6 ± 36.5) nm	(59.2 ± 25.3) nm	16	0.15
SiO_2AgNP/Si<1 0 0>60′	(134.7 ± 55.4) nm	(148.3 ± 18.4) nm	8	0.59
ZrO_2AgNP/Si<1 0 0>30′	(39.3 ± 30.0) nm	(34.4 ± 22.2) nm	19	0.77
ZrO_2AgNP/Si<1 0 0>60′	(163.0 ± 32.3) nm	(127.8 ± 27.7) nm	20	0.08

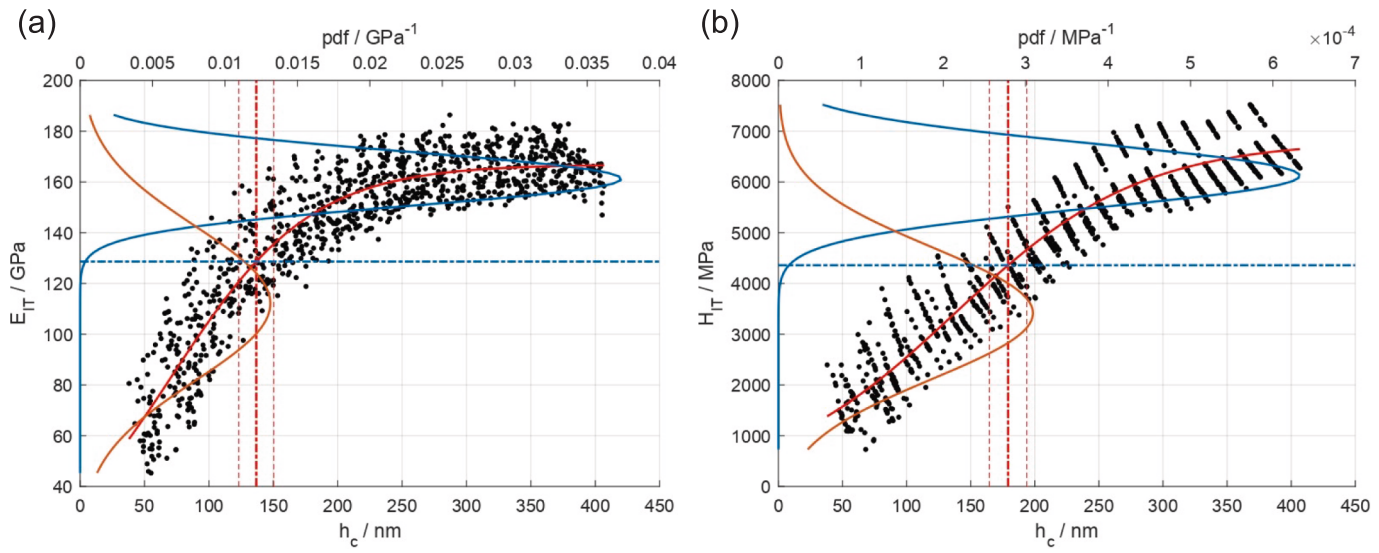


Fig. 4. Method application result for SiO_2AgNP/Si<1 0 0>with a deposition duration of 60′. Black points: measured data. Orange solid line: probability density function of the coating (transition layer) mechanical response. Blue solid line: probability density function of the substrate mechanical response. Red solid line: fitted $M = g(h_c)$. Blue dot-dashed line: M_2^*. Red dot-dashed line: $t_c = t_{M,2}^* = g^{-1}(M_2^*)$, with expanded uncertainty (95% confidence level) (red dashed lines). Deconvolution of (a) E_{IT} and (b) H_{IT}.

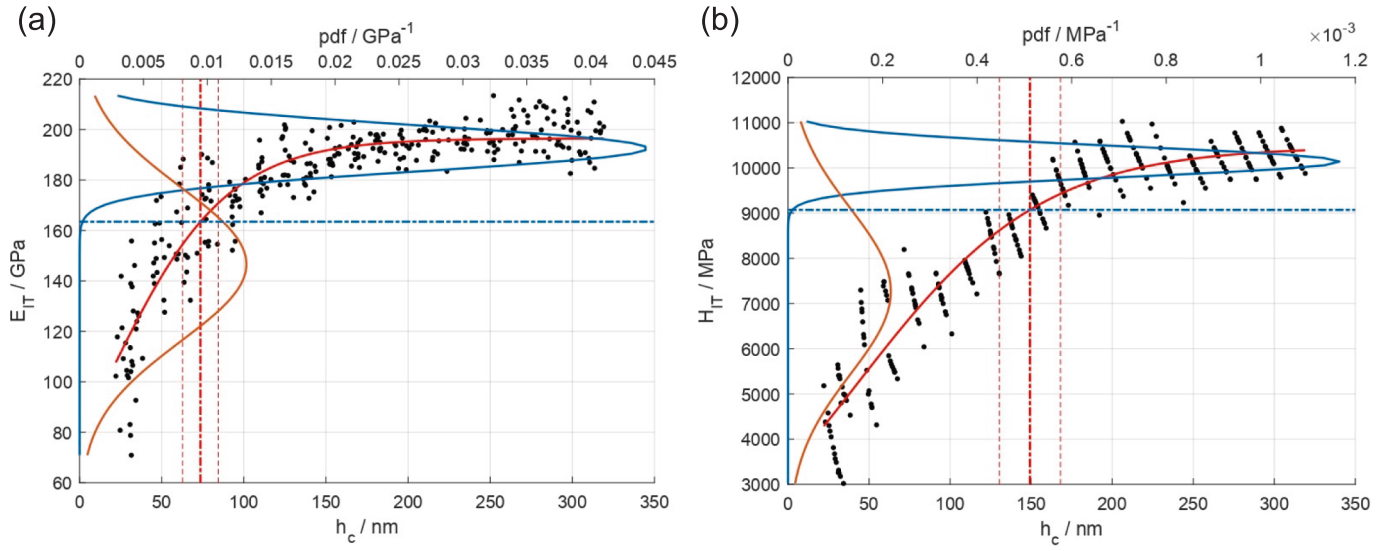


Fig. 5. Method application result for SiO_2AgNP/Si<1 0 0>with a deposition duration of 30′. Black points: measured data. Orange solid line: probability density function of the coating (transition layer) mechanical response. Blue solid line: probability density function of the substrate mechanical response. Red solid line: fitted $M = g(h_c)$. Blue dot-dashed line: M_2^*. Red dot-dashed line: $t_c = t_{M,2}^* = g^{-1}(M_2^*)$, with expanded uncertainty (95% confidence level) (red dashed lines). Deconvolution of (a) E_{IT} and (b) H_{IT}.

SiO_2AgNP/Si<1 0 0>30′, SiO_2AgNP/Si<1 0 0>60′, ZrO_2AgNP/Si<1 0 0>30′, and ZrO_2AgNP/Si<1 0 0>60′ in Sa values of 1 nm, 0.8 nm, 0.5 nm, and 0.45 nm.

Then, coatings were indented following the methodology outlined in Section 2.1. As discussed in Section 2.1, the particular interaction between the indentation force scale and the material response determines whether shallow indentation in the functional layer can be obtained. The minimum penetration depths for the four coatings (SiO_2AgNP/Si<1 0 0>30′, SiO_2AgNP/Si<1 0 0>60′, ZrO_2AgNP/Si<1 0 0>30′, and ZrO_2AgNP/Si<1 0 0>60′) were, respectively, 25 nm, 50 nm, 25 nm, and 30 nm. Since all the minimum penetration depths exceed 10% of the coating thickness (see Table 2), a simplified material model shall be used. Specifically, in line with the methodology outlined in Section 2.1, because no indentation data can be collected in the functional layer, a simpler model with a three-parameter logistic function, as in Eq. (5.1), and a GMM with two latent distributions were considered. The latter, in particular, accounts for the fact that only the interface and the substrate will contribute to the convolution, i.e., with respect to the model of Eq. (6), it results as $M \sim GMM(\boldsymbol{\mu}, \Sigma; \pi) = \pi_2 N(\mu_2, \sigma_2^2) + \pi_{1/2} N\left(\mu_{1/2}, \sigma_{1/2}^2\right)$. Accordingly, only the physical interface thickness will be evaluated. Such a limitation is strictly dependent on the used NHT^3 nanoindenter. However, the availability of an indentation platform capable of managing a maximum applied load smaller than 0.1 mN would overcome this technical limit, or the use of spherical indenters. Fig. 4 shows the deconvolution of the mechanical response for SiO_2AgNP/Si<1 0 0>with

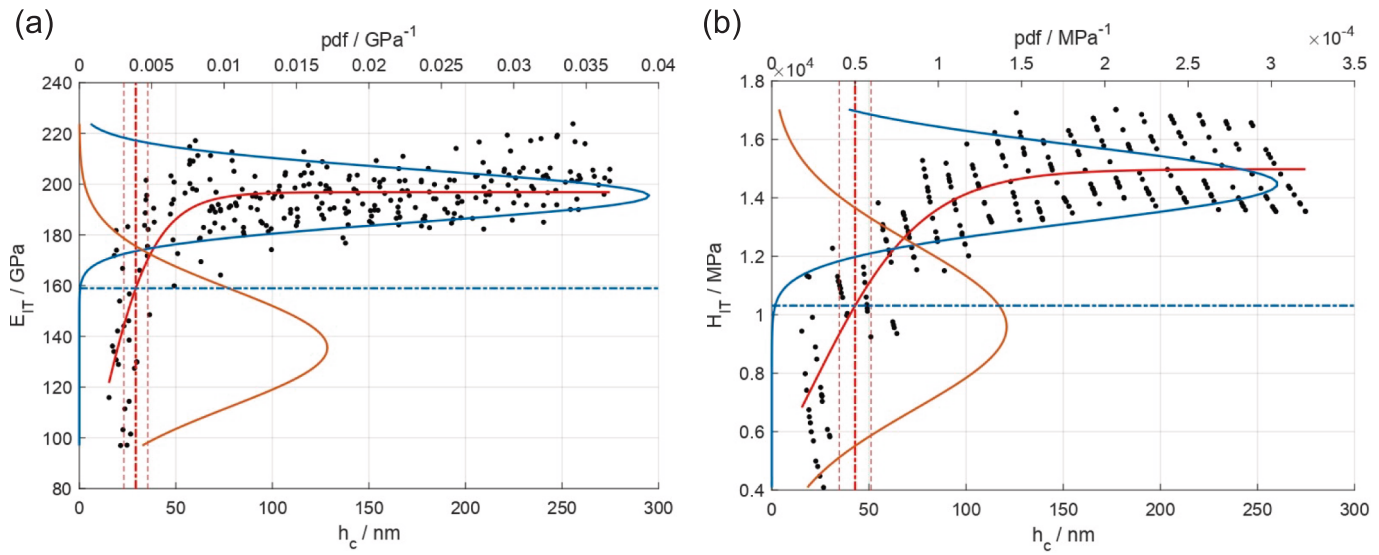


Fig. 6. Method application result for ZrO_2AgNP/Si<1 0 0>with a deposition duration of 30′. Black points: measured data. Orange solid line: probability density function of the coating (transition layer) mechanical response. Blue solid line: probability density function of the substrate mechanical response. Red solid line: fitted $M = g(h_c)$. Blue dot-dashed line: M_2^*. Red dot-dashed line: $t_c = t_{M,2}^* = g^{-1}(M_2^*)$, with expanded uncertainty (95% confidence level) (red dashed lines). Deconvolution of (a) E_{IT} and (b) H_{IT}.

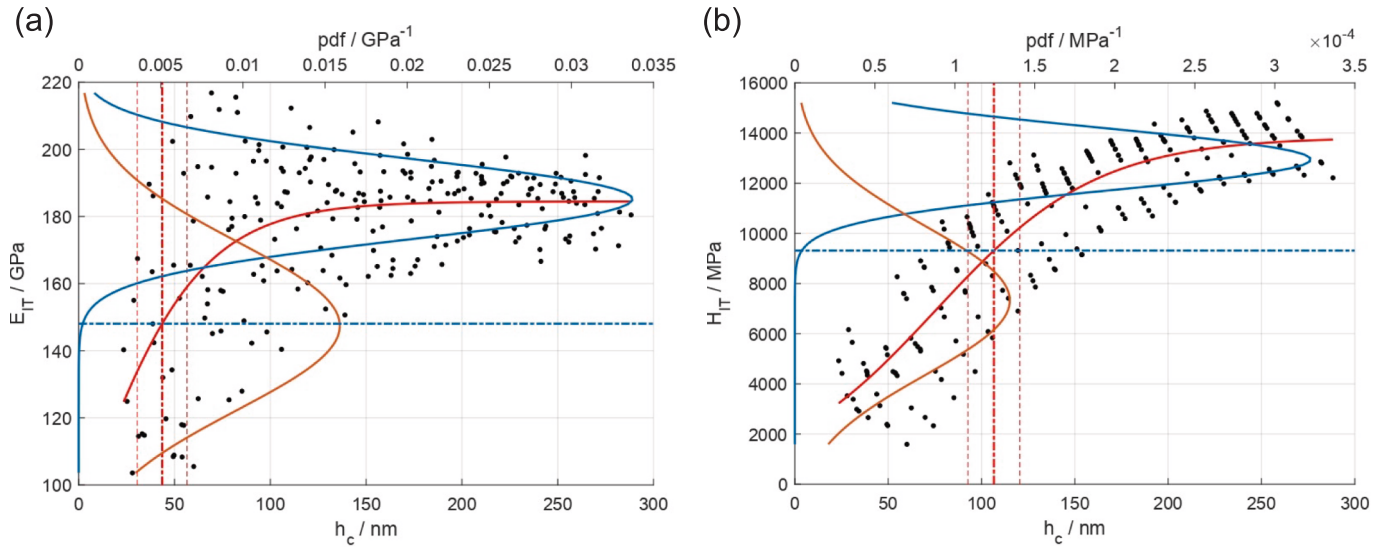


Fig. 7. Method application result for ZrO_2AgNP/Si<1 0 0>with a deposition duration of 60′. Black points: measured data. Orange solid line: probability density function of the coating (transition layer) mechanical response. Blue solid line: probability density function of the substrate mechanical response. Red solid line: fitted $M = g(h_c)$. Blue dot-dashed line: M_2^*. Red dot-dashed line: $t_c = t_{M,2}^* = g^{-1}(M_2^*)$, with expanded uncertainty (95% confidence level) (red dashed lines). Deconvolution of (a) E_{IT} and (b) H_{IT}.

a deposition duration of 60′, highlighting the quantiles M_i^* and the corresponding physical interface thickness $t_{M,i}^*$. Fig. 5, Fig. 6, and Fig. 7 report similar plots for the other three considered coatings. Goodness-of-fit diagnostic for the GMM are reported in the annex Table A1.

4.1. Critical analysis

Fig. 8 summarises the results of applying the thickness evaluation methodology and the uncertainty evaluation, respectively introduced in Section 2.1 and Section 3.2. The overlap of the error bars provides a graphical interpretation of the t-Student hypothesis test on the pairwise differences between the different methods. As can be appreciated, an average compatibility between the nanoindentation-based thickness measurement and other independent approaches can be seen. More in detail, it can be appreciated that the particular material system affects the accuracy e_{PGI-CS} depending on the mechanical characteristics considered, i.e., whether $t_{E,i}^*$, $t_{H,i}^*$ or $t_{DF,i}^*$ are evaluated. With reference to Fig. 4 and Fig. 5, Fig. 6, and Fig. 7, it can be immediately appreciated that the most accurate method for thickness evaluation is the one that leverages the mechanical characteristic that between the coating and the substrate presents the most significant difference. This is indeed beneficial for increasing the simplicity and robustness of the deconvolution of the mechanical response. In fact, SiO_2 and Si present a very similar indentation hardness with differences in the order of a half order of magnitude. Conversely, the indentation modulus increases of almost 200% from the SiO_2 coating to the Si, thus yielding better agreement in

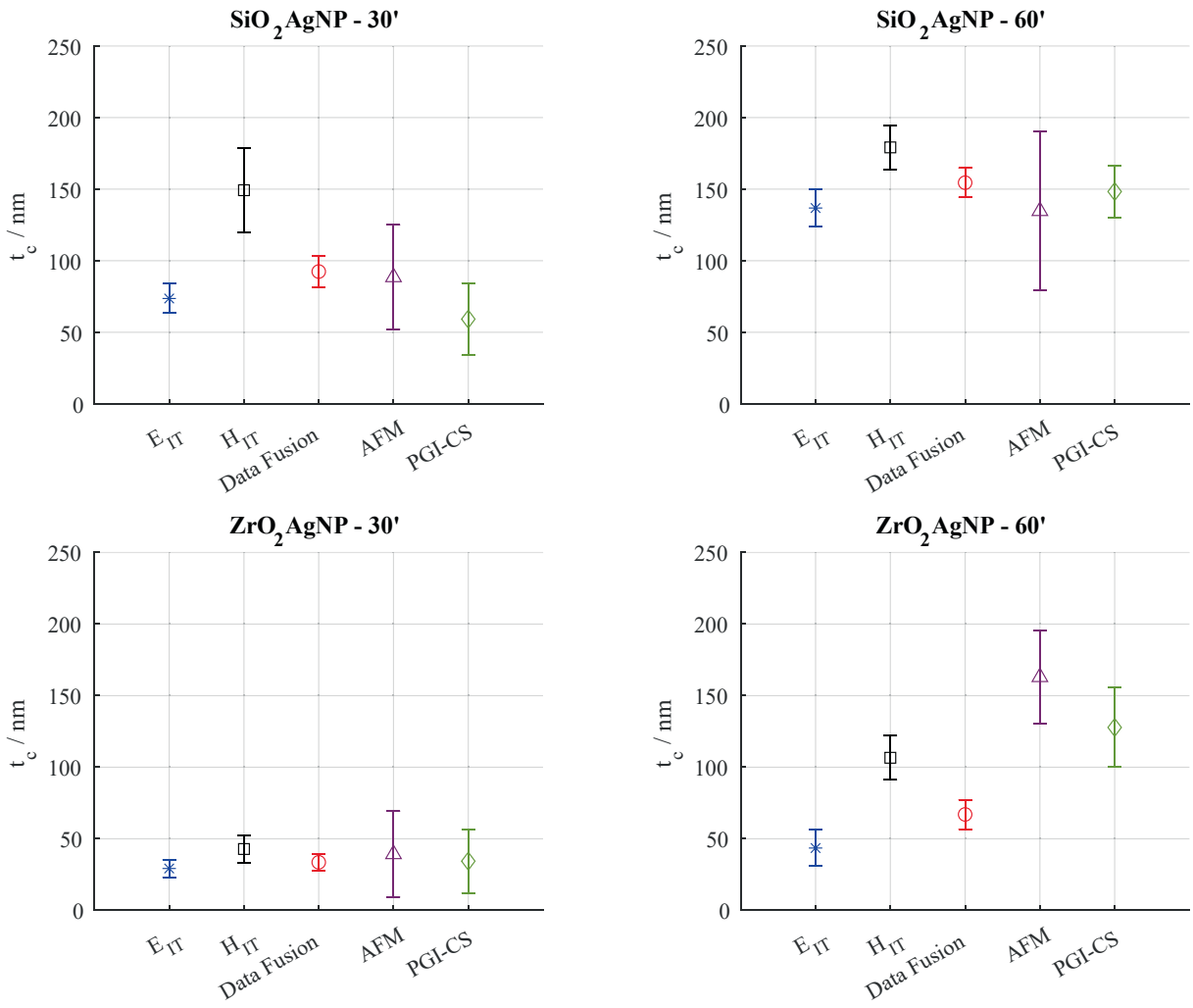


Fig. 8. Error bar plot with confidence interval at a 95% confidence level for the evaluated coating thickness (physical interface) based on nanoindentation-based method (using only the E_{IT}, the H_{IT}, or by Data fusion), and by directly traceable approaches, i.e. AFM and PGI-CS.

Table 3
Metrological characteristics of the nanoindentation-based coating thickness evaluation. Results in terms of measured thickness and expanded uncertainty (confidence level of 95%, k = 1.97, resulting from the very large available degrees of freedom), and relative uncertainty. Data related to SiO_2/Si<1 0 0> and PTFE + Pb/Bronze are provided to give evidence for thicker coatings [38].

Material	$t_c^* \pm U(t_c^*)$	$U(t_c^*)$%
SiO_2AgNP/Si<1 0 0>30′	$t_{E,2}^* = (73.6 \pm 10.3)$ nm	14.0%
SiO_2AgNP/Si<1 0 0>60′	$t_{E,2}^* = (136.8 \pm 12.8)$ nm	9.4%
ZrO_2AgNP/Si<1 0 0>30′	$t_{H,2}^* = (42.9 \pm 9.5)$ nm	22.1%
ZrO_2AgNP/Si<1 0 0>60′	$t_{H,2}^* = (106.6 \pm 15.5)$ nm	14.6%
SiO_2/Si<1 0 0>	$t_E^* = (542.0 \pm 84)$ nm	15.5%
PTFE + Pb/Bronze	$t_{DF}^* = (46.777 \pm 5.976)$ µm	12.8%

terms of accuracy between $t_{E,i}^*$ and the PGI-CS measurement. The situation is reversed for the ZrO_2/Si system. In fact, the largest difference is in the indentation hardness, which provides better accuracy. In particular, the large dispersion of the E_{IT} characterisation on the ZrO_2AgNP/Si<1 0 0>deposited for 60′ (see Fig. 7), generates a very poor accuracy of the associated $t_{E,i}^*$, as it can be appreciated in Fig. 8. Such large dispersion is due to the greater variability of material composition, specifically induced by larger AgNP clusters whose growth is promoted with longer deposition durations [48].

The metrological characteristics of the nanoindentation-based coating thickness are reported in Table 3 and in Table 4 for uncertainty and accuracy, respectively. In particular, the uncertainty $U(t_c^*)$, the relative uncertainty $U(t_c^*)$%, computed as the ratio between the uncertainty and the measured thickness t_c^*, the accuracy e_{PGI-CS}, and the absolute relative accuracy $e_{PGI-CS\%}$ are evaluated and reported. Results are provided by exploiting the mechanical response that allows for better deconvolution, i.e., the indentation modulus for the SiO_2/Si and the indentation hardness for the ZrO_2/Si. Details of the uncertainty budget are available in the annex from Table A10 to Table A13. Additionally, to provide a broader outlook on the metrological performances, additional data for thicker coatings are reported from [38]. As can be appreciated, an expanded relative uncertainty of about 15% results, independent of the measured thickness. Conversely, the relative accuracy is sensitive to the measured thickness. In particular, for ultra-thin coatings, i.e.$t_c < 100$ nm, a positive bias of about 24% results. On the other hand, for thicker coatings, the nanoindentation-based thickness measurement underestimates the thickness by about 8%. However, the bias is not statistically significant when tested with a *t*-test, with a 5% risk of error, as shown by the p-values reported in Table 4. The result is also due to the relatively large uncertainty of thickness measurement, both for the reference measurement and the nanoindentation method, which caters for the reproducibility. In fact, as it can be appreciated from

Table 4
Metrological characteristics of the nanoindentation-based coating thickness evaluation. Results in terms of accuracy and absolute relative accuracy, and significance of the bias tested by t-Student hypothesis test. Additional information on the t-Student test report the degrees of freedom, the uncertainty of the accuracy, obtained for a confidence level of 95% with following Eq. (23). Data related to SiO_2/Si<1 0 0> and PTFE + Pb/Bronze are provided to give evidence for thicker coatings [38].

Material	t_c^*	$e_{PGI-CS} \pm U(e_{PGI-CS})$	$\lvert e_{PGI-CS\%} \rvert$	ν	p-value
SiO_2AgNP/Si<1 0 0>30′	$t^*_{E,2} = 73.6$ nm	(14.4 ± 27.0) nm	24.3%	27	0.283
SiO_2AgNP/Si<1 0 0>60′	$t^*_{E,2} = 136.8$ nm	(−11.5 ± 22.0) nm	7.8%	45	0.299
ZrO_2AgNP/Si<1 0 0>30′	$t^*_{H,2} = 42.9$ nm	(8.5 ± 23.9) nm	24.6%	28	0.471
ZrO_2AgNP/Si<1 0 0>60′	$t^*_{H,2} = 106.6$ nm	(−21.2 ± 31.3) nm	16.6%	35	0.180
SiO_2/Si<1 0 0>	$t^*_E = 542.0$ nm	(−24.0 ± 90.8) nm	4.2%	16	0.583
PTFE + Pb/Bronze	$t^*_{DF} = 46.777$ µm	(−3.343 ± 21.4) µm	6.7%	22	0.749

the uncertainty tables, the major contribution comes from the regression residuals which accounts for coating composition and thickness inhomogeneity. Conversely, contributions from the GMM clustering are negligible (further details on clustering robustness are available in the annex).

Last, the effect of data fusion can be discussed, with reference to Fig. 8, on the metrological performances. Specifically, as reported in Table A14, the data fusion, as described in Section 2.1.1 produces a decrease in the relative uncertainty. Conversely, the effect on bias is highly dependent on the specific material system. For cases in which the deconvolution is suitably robust, such that $t^*_{M,i}$, for any M, provide accurate results, e.g. for SiO_2AgNP/Si<1 0 0>60′ (thanks to the larger thickness) and ZrO_2AgNP/Si<1 0 0>30′ (thanks to the larger difference in mechanical response between coating and substrate and the very small and isolated clusters of AgNP [48]), DF improves the accuracy. In any other case, i.e., when thicknesses estimated by different mechanical properties through nanoindentation have different orders of magnitude, the inverse variance weighting, being a competitive data fusion algorithm, cannot compensate systematic errors [62] and shall not be relied upon. Conversely, DF can be essential when further characterisation signals can be obtained from the coating, e.g. electrical contact resistance for conductive materials, not only to improve thickness measurements but also to gain insight into the material composition and homogeneity [38].

4.2. Limitations

The present work has developed an uncertainty evaluation for functional coatings thickness measurement by nanoindentation. However, some methodological and practical limitations can be highlighted.

Foremostly, a formal sensitivity analysis to instrumented indentation test parameters, such as loading and strain rate, and the indenter geometry is missing. The former might affect both the sigmoid fitting and the clustering. The latter, in the case a spherical indenter is used, would allow to obtain shallower indentations for the same load range, possibly enabling characterization in the first 10% of thickness, thus potentially affecting the sigmoid fitting and the clustering. The sensitivity analysis might achieve an optimization of the bias and uncertainty for the considered nanoindentation-based coating thickness measurement.

Secondly, a sensitivity analysis to sample and substrate properties is necessary to investigate applicability to coatings on soft substrates, and the effect of different surface roughness. Such an analysis might set limits for the applicability of the considered nanoindentation-based coating thickness measurement.

Last, it shall be noted that a calibrated reference artifact with high uniformity in composition and coating thickness over a wide range of thickness is not currently available. The development of such an artifact would allow, from the one hand, evaluating the metrological characteristics of the indentation-based method minimizing the effect of the reproducibility, and, on the other hand, to robustly benchmark different measurement method, if the artifact design overcomes the many limitations for the application of conventional coating thickness measurement methods.

5. Conclusions

This work provided a metrological assessment of nanoindentation-based coating thickness measurement. Primarily, the work successfully demonstrated the application of the method for coatings thinner than 100 nm, which find applications in critical sectors such as electronics and aerospace.

Also, the traceability of the methodology was discussed, and the main metrological characteristics, including measurement uncertainty and accuracy, were evaluated, with a particular focus on sensitivity to the measured thickness. The relative expanded uncertainty resulted in about 15% independently of the measured thickness. The bias, evaluated against directly traceable and independent methods such as interferometric contact stylus and atomic force microscopy, showed a relative magnitude dependent on the measured thickness, of about 24% for thicknesses smaller than 100 nm, and of about −8% for thicker coatings. However, the bias results to be not statistically significant.

The results showed the applicability of nanoindentation-based coating thickness measurement to industrial case studies over a wide range of thickness. Future works will investigate applicability to soft substrates and to application in quantum technologies based on ultra-low force, i.e. smaller than < 0.5 mN, nanoindentation.

Additionally, future works will address sensitivity studies on the effect of instrumented indentation test parameters, of the indenter geometry, which controls the contact mechanics, and of coating and substrate material and roughness on the thickness measurement. Also, future work will benchmark performance of several coating thickness measurement techniques by developing an appropriate reference material.

CRediT authorship contribution statement

Giacomo Maculotti: Writing – original draft, Visualization, Software, Methodology, Investigation, Formal analysis, Data curation, Conceptualization. **Luigi Ribotta:** Writing – review & editing, Validation, Investigation. **Gianfranco Genta:** Writing – review & editing, Validation, Formal analysis. **Maurizio Galetto:** Writing – review & editing, Validation, Supervision, Project administration, Funding acquisition.

Declaration of competing interest

The authors declare that they have no known competing financial interests or personal relationships that could have appeared to influence the work reported in this paper.

Acknowledgements

The authors would like to thank Prof. C. Balagna and Dr. F. Gattucci for providing the samples. This study was carried out within the MICS (Made in Italy – Circular and Sustainable) Extended Partnership and

received funding from the European Union Next-GenerationEU (PIANO NAZIONALE DI RIPRESA E RESILIENZA (PNRR) – MISSIONE 4 COMPONENTE 2, INVESTIMENTO 1.3 – D.D. 1551.11–10–2022, PE00000004). This manuscript reflects only the authors' views and opinions, neither the European Union northe European Commission can be considered responsible for them.

Annex.

.

Table A1
Goodness-of-fit diagnostics for the GMM deconvolution. Non-negative Likelihood (NNL), AIC and BIC scores.

Material	NNL	AIC	BIC
SiO_2AgNP/Si<1 0 0>30′	1292	2612	2593
SiO_2AgNP/Si<1 0 0>60′	4748	9530	9506
ZrO_2AgNP/Si<1 0 0>30′	2445	4917	4899
ZrO_2AgNP/Si<1 0 0>60′	2159	4345	4328

Table A2
Uncertainty Table for PGI-CS measurement of SiO_2AgNP/Si<1 0 0>30′.

Measurement (y)	Contribution (x_j)	$u^2(x_j)$/nm^2	ν_j	c_j/−	$u_j^2(y)$/nm^2
t_{PGI-CS} = 59.2 nm	Reproducibility:$s^2(t_{PGI-CS})$	147.168	19	1	146.168
	Traceability:$\left(\frac{U_{CMC,95\%}}{2}\right)^2$	0.410	130	1	0.410
				$\boldsymbol{u_c^2(y)}$	146.577 nm^2
				$\boldsymbol{u_c(y)}$	12.1 nm
				$\boldsymbol{\nu}$	19
				$\boldsymbol{k}$	2.09
				$\boldsymbol{U(y)}$	25.3 nm

Table A3
Uncertainty Table for PGI-CS measurement of SiO_2AgNP/Si<1 0 0>60′.

Measurement (y)	Contribution (x_j)	$u^2(x_j)$/nm^2	ν_j	c_j/−	$u_j^2(y)$/nm^2
t_{PGI-CS} = 148.3 nm	Reproducibility:$s^2(t_{PGI-CS})$	76.913	19	1	76.913
	Traceability:$\left(\frac{U_{CMC,95\%}}{2}\right)^2$	0.706	130	1	0.706
				$\boldsymbol{u_c^2(y)}$	77.618 nm^2
				$\boldsymbol{u_c(y)}$	8.8 nm
				$\boldsymbol{\nu}$	19
				$\boldsymbol{k}$	2.09
				$\boldsymbol{U(y)}$	18.4 nm

Table A4
Uncertainty Table for PGI-CS measurement of ZrO_2AgNP/Si<1 0 0>30′.

Measurement (y)	Contribution (x_j)	$u^2(x_j)$/nm^2	ν_j	c_j/−	$u_j^2(y)$/nm^2
t_{PGI-CS} = 34.4 nm	Reproducibility:$s^2(t_{PGI-CS})$	112.572	19	1	112.572
	Traceability:$\left(\frac{U_{CMC,95\%}}{2}\right)^2$	0.336	130	1	0.336
				$\boldsymbol{u_c^2(y)}$	112.908 nm^2
				$\boldsymbol{u_c(y)}$	10.6 nm
				$\boldsymbol{\nu}$	19
				$\boldsymbol{k}$	2.09
				$\boldsymbol{U(y)}$	22.2 nm

Table A5
Uncertainty Table for PGI-CS measurement of ZrO_2AgNP/Si<1 0 0>60′.

Measurement (y)	Contribution (x_j)	$u^2(x_j)$/nm^2	ν_j	c_j/−	$u_j^2(y)$/nm^2
t_{PGI-CS} = 127.8 nm	Reproducibility:$s^2(t_{PGI-CS})$	175.033	19	1	175.033
	Traceability:$\left(\frac{U_{CMC,95\%}}{2}\right)^2$	0.624	130	1	0.624
				$\boldsymbol{u_c^2(y)}$	175.657 nm^2
				$\boldsymbol{u_c(y)}$	13.3 nm
				$\boldsymbol{\nu}$	19
				$\boldsymbol{k}$	2.09
				$\boldsymbol{U(y)}$	27.7 nm

Table A6
Uncertainty Table for AFM measurement of SiO_2AgNP/Si<1 0 0>30′.

Measurement (y)	Contribution (x_j)	$u^2(x_j)$/nm^2	ν_j	c_j/−	$u_j^2(y)$/nm^2
t_{AFM} = 88.5 nm	Reproducibility:$s^2(\overline{z_{coating}})$	199.527	5	1	199.527
	Reproducibility:$s^2(\overline{z_{substrate}})$	38.507	5	1	38.507
	Noise	0.0064	100	1	0.0064
				$\boldsymbol{u_c^2(y)}$	238.040 nm^2
				$\boldsymbol{u_c(y)}$	15.4 nm
				$\boldsymbol{\nu}$	7
				$\boldsymbol{k}$	2.36
				$\boldsymbol{U(y)}$	36.5 nm

Table A7
Uncertainty Table for AFM measurement of SiO_2AgNP/Si<1 0 0>60′.

Measurement (y)	Contribution (x_j)	$u^2(x_j)$/nm^2	ν_j	c_j/−	$u_j^2(y)$/nm^2
t_{AFM} = 134.7 nm	Reproducibility:$s^2(\overline{z_{coating}})$	471.407	5	1	471.407
	Reproducibility:$s^2(\overline{z_{substrate}})$	40.042	5	1	40.042
	Noise	0.0064	100	1	0.0064
				$\boldsymbol{u_c^2(y)}$	511.755 nm^2
				$\boldsymbol{u_c(y)}$	22.6 nm
				$\boldsymbol{\nu}$	6
				$\boldsymbol{k}$	2.45
				$\boldsymbol{U(y)}$	55.4 nm

Table A8
Uncertainty Table for AFM measurement of ZrO_2AgNP/Si<1 0 0>30′.

Measurement (y)	Contribution (x_j)	$u^2(x_j)$/nm^2	ν_j	c_j/−	$u_j^2(y)$/nm^2
t_{AFM} = 39.3 nm	Reproducibility:$s^2(\overline{z_{coating}})$	132.540	5	1	132.540
	Reproducibility:$s^2(\overline{z_{substrate}})$	37.002	5	1	37.002
	Noise	0.0064	100	1	0.0064
				$\boldsymbol{u_c^2(y)}$	169.548 nm^2
				$\boldsymbol{u_c(y)}$	13.7 nm
				$\boldsymbol{\nu}$	8
				$\boldsymbol{k}$	2.31
				$\boldsymbol{U(y)}$	30.0 nm

Table A9
Uncertainty Table for AFM measurement of ZrO_2AgNP/Si<1 0 0>60′.

Measurement (y)	Contribution (x_j)	$u^2(x_j)$/nm^2	ν_j	c_j/−	$u_j^2(y)$/nm^2
t_{AFM} = 163.0 nm	Reproducibility:$s^2\left(\overline{z_{coating}}\right)$	149.002	5	1	149.002
	Reproducibility:$s^2\left(\overline{z_{substrate}}\right)$	38.002	5	1	38.002
	Noise	0.0064	100	1	0.0064
				$\boldsymbol{u_c^2(y)}$	187.010 nm^2
				$\boldsymbol{u_c(y)}$	13.7 nm
				$\boldsymbol{\nu}$	7
				$\boldsymbol{k}$	2.36
				$\boldsymbol{U(y)}$	32.3 nm

Table A10
Uncertainty Table for nanoindentation measurement of SiO_2AgNP/Si<1 0 0>30′.

Measurement (y)	Contribution (x_j)	$u^2(x_j)$	ν_j	c_j	$u_j^2(y)$/nm^2
$t^*_{E,2}$ = 73.6 nm	Parameters:Σ_ϑ	3.240 nm^2	317	1	3.240
	Traceability:$u^2(E)$	2.681 GPa^2	49	1.3425 nm/GPa	4.832
	Sample uniformity – reproducibility:*MSE*	8.037 GPa^2	317	1.3425 nm/GPa	14.486
	Reproducibility:$u^2(h)$	4.68 nm^2	15	1	4.680
	GMM reproducibility:$u^2_{GMM,reprod}$	0.018 nm^2	99	1	0.018
	GMM initialization $u^2_{EM,init}$	0.030	99	1	0.030
				$\boldsymbol{u_c^2(y)}$	27.286 nm^2
				$\boldsymbol{u_c(y)}$	5.2 nm
				$\boldsymbol{\nu_t}$	283
				$\boldsymbol{k_t}$	1.97
				$\boldsymbol{U(y)}$	10.3 nm

Table A11
Uncertainty Table for nanoindentation measurement of SiO_2AgNP/Si<1 0 0>60′.

Measurement (y)	Contribution (x_j)	$u^2(x_j)$	ν_j	c_j	$u_j^2(y)$/nm^2
$t^*_{E,2}$ = 136.8 nm	Parameters:Σ_ϑ	1.570 nm^2	317	1	1.570
	Traceability:$u^2(E)$	1.643 GPa^2	49	1.8225 nm/GPa	5.457
	Sample uniformity – reproducibility:*MSE*	9.142 GPa^2	317	1.8225 nm/GPa	30.364
	Reproducibility:$u^2(h)$	4.680 nm^2	15	1	4.680
	GMM reproducibility:$u^2_{GMM,reprod}$	0.038 nm^2	99	1	0.038
	GMM initialization $u^2_{EM,init}$	0.403	99	1	0.403
				$\boldsymbol{u_c^2(y)}$	42.512 nm^2
				$\boldsymbol{u_c(y)}$	6.5 nm
				$\boldsymbol{\nu_t}$	362
				$\boldsymbol{k_t}$	1.97
				$\boldsymbol{U(y)}$	12.8 nm

Table A12
Uncertainty Table for nanoindentation measurement of ZrO_2AgNP/Si<1 0 0>30′.

Measurement (y)	Contribution (x_j)	$u^2(x_j)$	ν_j	c_j	$u_j^2(y)$/nm^2
$t^*_{H,2}$ = 42.9 nm	Parameters:Σ_ϑ	2.010 nm^2	317	1	2.010
	Traceability:$u^2(H)$	0.096 GPa^2	49	8.800 nm/GPa	7.408
	Sample uniformity – reproducibility:*MSE*	0.115 GPa^2	317	8.800 nm/GPa	8.921
	Reproducibility:$u^2(h)$	4.680 nm^2	15	1	4.680
	GMM reproducibility:$u^2_{GMM,reprod}$	0.055 nm^2	99	1	0.055
	GMM initialization $u^2_{EM,init}$	0.083	99	1	0.083
				$\boldsymbol{u_c^2(y)}$	23.158 nm^2
				$\boldsymbol{u_c(y)}$	4.8 nm
				$\boldsymbol{\nu_t}$	189
				$\boldsymbol{k_t}$	1.97
				$\boldsymbol{U(y)}$	9.49 nm

Table A13
Uncertainty Table for nanoindentation measurement of ZrO_2AgNP/Si<1 0 0>60′.

Measurement (y)	Contribution (x_j)	$u^2(x_j)$	ν_j	c_j	$u_j^2(y)$/nm^2
$t^*_{H,2} = 106.6$ nm	Parameters:Σ_ϑ	6.420 nm^2	317	1	6.420
	Traceability:$u^2(H)$	0.078 GPa^2	49	14.300 nm/GPa	15.964
	Sample uniformity – reproducibility:*MSE*	0.169 GPa^2	317	14.300 nm/GPa	34.578
	Reproducibility:$u^2(h)$	4.680 nm^2	15	1	4.680
	GMM reproducibility:$u^2_{GMM,reprod}$	0.091 nm^2	99	1	0.091
	GMM initialization $u^2_{EM,init}$	0.563	99	1	0.563
				$\boldsymbol{u}_c^2(\boldsymbol{y})$	62.296 nm^2
				$\boldsymbol{u}_c(\boldsymbol{y})$	7.9 nm
				$\boldsymbol{\nu}_t$	367
				$\boldsymbol{k}_t$	1.97
				$\boldsymbol{U}(\boldsymbol{y})$	15.5 nm

Table A14
Metrological characteristics of the nanoindentation-based coating thickness evaluation. Results in terms of measured thickness and expanded uncertainty (confidence level of 95%), relative uncertainty, accuracy and absolute relative accuracy, and significance of the bias tested by t-Student hypothesis test. Thickness evaluation performed using data fusion.

Material	$t^*_{DF,2} \pm U\left(t^*_{DF,2}\right)$	$U\left(t^*_{M,2}\right)$%	e_{PGI-CS}	$\lvert e_{PGI-CS\%}\rvert$	p-value
SiO_2AgNP/Si<1 0 0>30′	(81.8 ± 10.9) nm	13.3%	22.6 nm	38.2%	0.096
SiO_2AgNP/Si<1 0 0>60′	(154.5 ± 10.2) nm	6.6%	6.2 nm	4.2%	0.545
ZrO_2AgNP/Si<1 0 0>30′	(33.6 ± 5.6) nm	16.6%	−0.8 nm	2.3%	0.943
ZrO_2AgNP/Si<1 0 0>60′	(67.0 ± 10.3) nm	15.4%	−60.7 nm	47.5%	<0.001

Data availability

Raw data and code implementing the thickness measurement method are available at https://doi.org/10.5281/zenodo.18921964.

References

[1] A.A.G. Bruzzone, H.L. Costa, P.M. Lonardo, D.A. Lucca, Advances in engineered surfaces for functional performance, CIRP Ann. Manuf. Technol. 57 (2008) 750–769, https://doi.org/10.1016/j.cirp.2008.09.003.

[2] M.D. Tyona, A comprehensive study of spin coating as a thin film deposition technique and spin coating equipment, Adv. Mater. Res. 2 (2013) 181–193, https://doi.org/10.12989/amr.2013.2.4.181.

[3] Z. Yang, J. Su, J. Wang, X. Li, F. Li, J. Hu, N. Chen, Z. Tao, D. Yang, D. Wang, Q. Zhu, Y. Liao, Z. Lu, Spin-coating fabrication of high-yield and uniform organic thin-film transistors via a primer template growth, Aggregate 6 (2025), https://doi.org/10.1002/agt2.661.

[4] A. Zaccone, Quantum confinement theory of ultra-thin films: electronic, thermal and superconducting properties, Journal of Physics: Materials 8 (2025) 031001, https://doi.org/10.1088/2515-7639/adc83f.

[5] T.V. Anitha, K. Gadha Menon, K. Venugopal, T.V. Vimalkumar, Investigating the role of film thickness on the physical properties of sol-gel coated CuO thin films: discussing its potentiality in optoelectronic applications, Mater. Sci. Eng. B 299 (2024) 116960, https://doi.org/10.1016/j.mseb.2023.116960.

[6] K. Bewilogua, G. Bräuer, A. Dietz, J. Gäbler, G. Goch, B. Karpuschewski, B. Szyszka, Surface technology for automotive engineering, CIRP Ann. Manuf. Technol. 58 (2009) 608–627, https://doi.org/10.1016/j.cirp.2009.09.001.

[7] J. Fleischer, D. Ceglarek, J. Franke, C. Herrmann, Production technologies and systems for electric mobility, CIRP Ann. 74 (2025) 1047–1072, https://doi.org/10.1016/j.cirp.2025.05.001.

[8] M. Hołyńska, A. Tighe, C. Semprimoschnig, Coatings and Thin Films for Spacecraft Thermo-Optical and Related Functional applications, Adv. Mater. Interfaces 5 (2018) 1–20, https://doi.org/10.1002/admi.201701644.

[9] K.D. Bouzakis, N. Michailidis, G. Skordaris, E. Bouzakis, D. Biermann, R. M'Saoubi, Cutting with coated tools: Coating technologies, characterization methods and performance optimization, CIRP Ann. Manuf. Technol. 61 (2012) 703–723, https://doi.org/10.1016/j.cirp.2012.05.006.

[10] G. Maculotti, E. Goti, G. Genta, L. Mazza, M. Galetto, Comprehensive mechanical and tribological characterization of metal-polymer PTFE+Pb/Bronze coating by in-situ electrical contact resistance measurement augmented tribo-mechanical tests, Tribol. Int. 193 (2024) 109397, https://doi.org/10.1016/j.triboint.2024.109397.

[11] M. Conte, A. Igartua, Study of PTFE composites tribological behavior, Wear 296 (2012) 568–574, https://doi.org/10.1016/j.wear.2012.08.015.

[12] A. Mura, H. Wang, F. Adamo, J. Kong, Graphene coatings to enhance tribological performance of steel, Mech. Adv. Mater. Struct. (2019) 1–8, https://doi.org/10.1080/15376494.2019.1582825.

[13] M. Patel, A.K. Karamalidis, Germanium: a review of its US demand, uses, resources, chemistry, and separation technologies, Sep. Purif. Technol. 275 (2021) 118981, https://doi.org/10.1016/j.seppur.2021.118981.

[14] P.C. Moura, S. Sério, Recent applications and Future Trends of Nanostructured Thin Films-based Gas Sensors Produced by Magnetron Sputtering, Coatings 14 (2024) 1214, https://doi.org/10.3390/coatings14091214.

[15] D. Liu, R. Jiao, C. Sun, Y. Wang, Effects of Substrates on the Performance of Pt Thin-Film Resistance Temperature Detectors, Coatings 14 (2024) 969, https://doi.org/10.3390/coatings14080969.

[16] Y. Wang, E.J. Terrell, Influence of coating thickness and substrate elasticity on the tribological performance of PEEK coatings, Wear 303 (2013) 255–261, https://doi.org/10.1016/j.wear.2013.03.036.

[17] H. Asgari, M.R. Toroghinejad, M.A. Golozar, Effect of coating thickness on modifying the texture and corrosion performance of hot-dip galvanized coatings, Curr. Appl Phys. 9 (2009) 59–66, https://doi.org/10.1016/j.cap.2007.10.090.

[18] Y. Chen, Z. Shu, S. Zhang, P. Zeng, H. Liang, M. Zheng, H. Duan, Sub-10 nm fabrication: methods and applications, International Journal of Extreme Manufacturing 3 (2021) 032002, https://doi.org/10.1088/2631-7990/ac087c.

[19] A.R. Kirmani, H. Chen, C.M. Stafford, E.G. Bittle, L.J. Richter, Coating Thickness Controls Crystallinity and Enables Homoepitaxial growth of Ultra-Thin-Channel Blade-Coated In_2O_3 Transistors, Adv. Electron. Mater. 6 (2020), https://doi.org/10.1002/aelm.202000354.

[20] F. Anwar, R. Mahbub, R.A. Coutu, Thin film materials for room temperature quantum applications, IEEE Trans. Quantum Eng. 4 (2023) 1–10, https://doi.org/10.1109/TQE.2023.3322342.

[21] M. Jannesar, G.R. Jafari, S. Vasheghani Farahani, S. Moradi, Thin film thickness measurement by the conductivity theory in the framework of born approximation, Thin Solid Films 562 (2014) 372–376, https://doi.org/10.1016/j.tsf.2014.04.070.

[22] J.R. Velasquez-Ordoñez, J. Rivera-Taco, D.G. Pacheco-Salazar, J.A.H. Coaquira, J. L. Maldonado, J.A. Guerra, P. Llontop, P.C. Morais, F.F.H. Aragón, Impact of the thickness on the optical and electronic and structural properties of sputtered Cu2S thin films, J. Appl. Phys. 135 (2024), https://doi.org/10.1063/5.0191049.

[23] S.H. Fawaeer, W.M. Al-Qaisi, V. Sedláková, M.S. Mousa, A. Knápek, D. Sobola, Substrate-temperature-driven phase stabilization and strain modulation in $BiFeO_3$/Ti/Si heterostructures for scalable silicon integration, J. Alloys Compd. 1047 (2025) 184949, https://doi.org/10.1016/j.jallcom.2025.184949.

[24] S.H. Fawaeer, V. Horník, W.M. Al-Qaisi, V. Sedláková, M.S. Mousa, A. Knápek, D. Sobola, Oxygen-pressure-tuned phase stability, microstructure, and magnetic properties of $BiFeO_3$ films on titanium-buffered silicon, Surf. Interfaces 86 (2026) 108769, https://doi.org/10.1016/j.surfin.2026.108769.

[25] Y. Akiyama, A. Kikuchi, M. Yamato, T. Okano, Ultrathin poly(*N*-isopropylacrylamide) grafted layer on polystyrene surfaces for cell adhesion/detachment control, Langmuir 20 (2004) 5506–5511, https://doi.org/10.1021/la036139f.

[26] D.L. Huber, R.P. Manginell, M.A. Samara, B.-I. Kim, B.C. Bunker, Programmed adsorption and release of proteins in a microfluidic device, Science 301 (2003) (1979) 352–354, https://doi.org/10.1126/science.1080759.
[27] C. Balagna, R. Francese, S. Perero, D. Lembo, M. Ferraris, Nanostructured composite coating endowed with antiviral activity against human respiratory viruses deposited on fibre-based air filters, Surf. Coat. Technol. 409 (2021) 126873, https://doi.org/10.1016/j.surfcoat.2021.126873.
[28] Z. Kheradmand, T. Mohammadi, G.I.T. Mukete, Biocompatible coatings for composite medical implants: enhancing integration and performance, J. Compos. Compd. 5 (2023), https://doi.org/10.61186/jcc.5.4.4.
[29] W. Giurlani, E. Berretti, M. Innocenti, A. Lavacchi, Measuring the thickness of metal coatings: a review of the methods, Coatings 10 (2020) 1211, https://doi.org/10.3390/coatings10121211.
[30] A. Kondi, E.-M. Papia, V. Constantoudis, D. Nioras, I. Syngelakis, C. Aivalioti, E. Aperathitis, E. Gogolides, Measurement of thickness of thin coatings on rough substrates via computational analysis of SEM images, Micro Nano Eng. 28 (2025) 100315, https://doi.org/10.1016/j.mne.2025.100315.
[31] P. Nestler, C.A. Helm, Determination of refractive index and layer thickness of nm-thin films via ellipsometry, Opt. Express 25 (2017) 27077, https://doi.org/10.1364/OE.25.027077.
[32] G. Goch, H. Prekel, S. Patzelt, G. Ströbel, D.A. Lucca, H.R. Stock, A. Mehner, Non-destructive and non-contact determination of layer thickness and thermal properties of PVD and sol-gel layers by photothermal methods, CIRP Ann. Manuf. Technol. 53 (2004) 471–474, https://doi.org/10.1016/S0007-8506(07)60742-2.
[33] P. Liu, K. Yi, H. Sohn, Estimation of silicon wafer coating thickness using ultrasound generated by femtosecond laser, J. Nondestruct. Eval. Diagn. Progn. Eng. Syst. 4 (2021), https://doi.org/10.1115/1.4047673.
[34] L.M. Dingemans, V.M. Papadakis, P. Liu, A.J.L. Adam, R.M. Groves, Quantitative coating thickness determination using a coefficient-independent hyperspectral scattering model, J. Eur. Opt. Soc.-Rapid Publ. 13 (2017) 40, https://doi.org/10.1186/s41476-017-0068-2.
[35] J.T. Dong, R.S. Lu, Sensitivity analysis of thin-film thickness measurement by vertical scanning white-light interferometry, Appl. Opt. 51 (2012) 5668–5675, https://doi.org/10.1364/AO.51.005668.
[36] Y.-M. Choi, H. Yoo, D. Kang, Large-area thickness measurement of transparent multi-layer films based on laser confocal reflection sensor, Measurement 153 (2020) 107390, https://doi.org/10.1016/j.measurement.2019.107390.
[37] Z. Li, U. Brand, T. Ahbe, Step height measurement of microscale thermoplastic polymer specimens using contact stylus profilometry, Precis. Eng. 45 (2016) 110–117, https://doi.org/10.1016/j.precisioneng.2016.02.001.
[38] G. Genta, G. Maculotti, Thin coatings thickness measurement by augmented nanoindentation data fusion, CIRP Ann. 73 (2024) 409–412, https://doi.org/10.1016/j.cirp.2024.04.093.
[39] D.A. Lucca, K. Herrmann, M.J. Klopfstein, Nanoindentation: measuring methods and applications, CIRP Ann. Manuf. Technol. 59 (2010) 803–819, https://doi.org/10.1016/j.cirp.2010.05.009.
[40] ISO 14577-1:2015 Metallic materials — Instrumented indentation test for hardness and material parameters - Part 1: Test method. ISO, Genève.
[41] N.M. Jennett, A.S. Maxwell, K. Lawrence, L.N. McCartney, R. Hunt, J. Koskinen, J. Meneve, W. Wegener, T. Muukkonen, F. Rossi, N. Gibson, Zhihui Xu, A.J. Bushb, S. A. Brookes, C.K. Herrmann, B. Bellaton, R. Consiglio, F. Augereau, K.D. Schneider, T. Chudoba, Indicoat Final Report. Determination of Hardness and Modulus of Thin Films and Coatings by Nanoindentation, 2001.
[42] S.J. Bull, Nanoindentation of coatings, J. Phys. D Appl. Phys. 38 (2005) R393–R413, https://doi.org/10.1088/0022-3727/38/24/R01.
[43] E.S. Puchi-Cabrera, M.H. Staia, A. Iost, Modeling the composite hardness of multilayer coated systems, Thin Solid Films 578 (2015) 53–62, https://doi.org/10.1016/j.tsf.2015.01.070.
[44] L. Lorenz, T. Chudoba, S. Makowski, M. Zawischa, F. Schaller, V. Weihnacht, Indentation modulus extrapolation and thickness estimation of ta-C coatings from nanoindentation, J. Mater. Sci. 56 (2021) 18740–18748, https://doi.org/10.1007/s10853-021-06448-2.
[45] A.P. Dempster, N.M. Laird, D.B. Rubin, Maximum likelihood from incomplete data via the EM algorithm, J. R. Stat. Soc. Ser. B: Methodol. 39 (1977) 1–38.
[46] K.P. Murphy, Machine Learning: A Probabilistic Perspective, The MIT Press, Cambridge, MA, 2012 doi: 10.1007/978-94-011-3532-0_2.
[47] M. Ferraris, C. Balagna, S. Perero, WO2019082001 - Method for the Application of an Antiviral Coating to a Substrate and Relative Coating, 2017.
[48] L. Giorio, G. Maculotti, F. Gattucci, G. Genta, C. Balagna, M. Galetto, Topographical and mechanical properties of sputtered composite coatings with silver nanoparticles for functional surfaces, Mater. TodayCommun. 51 (2026), https://doi.org/10.1016/j.mtcomm.2026.114894.
[49] C. Balagna, S. Perero, E. Percivalle, E.V. Nepita, M. Ferraris, Virucidal effect against coronavirus SARS-CoV-2 of a silver nanocluster/silica composite sputtered coating, Open Ceram. 1 (2020) 100006, https://doi.org/10.1016/j.oceram.2020.100006.
[50] A. Luceri, R. Francese, S. Perero, D. Lembo, M. Ferraris, C. Balagna, Antibacterial and antiviral activities of silver nanocluster/silica composite coatings deposited onto air filters, ACS Appl. Mater. Interfaces 16 (2024) 3955–3965, https://doi.org/10.1021/acsami.3c13843.
[51] D. Arthur, S. Vassilvitskii, K-means++: The advantages of careful seeding, in: Proceedings of the Annual ACM-SIAM Symposium on Discrete Algorithms, Association for Computing Machinery, 2007, pp. 1027–1035.
[52] ISO 14577-2:2015 Metallic Materials-Instrumented Indentation Test for Hardness and Materials Parameters-Part 2: Verification and Calibration of Testing Machines, ISO, Genève.
[53] G. Maculotti, G. Genta, M. Galetto, An uncertainty-based quality evaluation tool for nanoindentation systems, Measurement 225 (2024) 113974, https://doi.org/10.1016/j.measurement.2023.113974.
[54] G. Maculotti, L. Giorio, G. Genta, M. Galetto, Metrological comparison of indirect calibration methods for nanoindentation: a bootstrap-based approach, Materials 18 (2025), https://doi.org/10.3390/ma18184382.
[55] G. Maculotti, L. Giorio, G. Genta, M. Galetto, Code for Bootstrap simulation of nanoindentation data, 2025, doi: 10.5281/zenodo.17054598.
[56] JCGM100:2008 Evaluation of measurement data — Guide to the expression of uncertainty in measurement (GUM), JCGM, Sèvres, France, doi: 10.1373/clinchem.2003.030528.
[57] R. Cagliero, G. Barbato, G. Maizza, G. Genta, Measurement of elastic modulus by instrumented indentation in the macro-range: uncertainty evaluation, Int. J. Mech. Sci. 101–102 (2015) 161–169, https://doi.org/10.1016/j.ijmecsci.2015.07.030.
[58] G. Barbato, G. Genta, R. Cagliero, M. Galetto, M.J. Klopfstein, D.A. Lucca, R. Levi, Uncertainty evaluation of indentation modulus in the nano-range : contact stiffness contribution, CIRP Ann. Manuf. Technol. 66 (2017) 495–498, https://doi.org/10.1016/j.cirp.2017.04.060.
[59] L. Ribotta, E. Destefano, A. Guendouli, A. Giura, R. Bellotti, M. Zucco, Metrological Confirmation of the Stylus Profilometer Taylor Hobson Form Talysurf PGI Novus S 10 - RT-2024-14, 2023, https://hdl.handle.net/11696/80999 (accessed January 13, 2026).
[60] ISO 5436-1:2001 Geometrical Product Specifications (GPS). Surface Texture: Profile method; Measurement Standards - Part 1: Material Measures, ISO, Genève.
[61] L. Ribotta, A. Delvallée, E. Cara, R. Bellotti, A. Giura, I. De Carlo, M. Fretto, W. Knulst, R. Koops, B. Torre, Z. Saghi, L. Boarino, AFM interlaboratory comparison for nanodimensional metrology on silicon nanowires, Meas. Sci. Technol. 35 (2024) 105014, https://doi.org/10.1088/1361-6501/ad5e9f.
[62] F. Franceschini, M. Galetto, D. Maisano, L. Mastrogiacomo, Combining multiple large volume metrology systems: competitive versus cooperative data fusion, Precis. Eng. 43 (2016) 514–524, https://doi.org/10.1016/j.precisioneng.2015.09.014.